



# A simple one-pot strategy to platinum–palladium@palladium core–shell nanostructures with high electrocatalytic activity



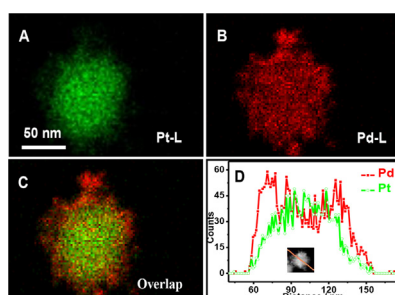
Jing-Jing Lv, Jie-Ning Zheng, Ying-Ying Wang, Ai-Jun Wang\*, Li-Li Chen, Jiu-Ju Feng\*

College of Geography and Environmental Science, College of Chemistry and Life Science, Zhejiang Normal University, Jinhua 321004, China

## HIGHLIGHTS

- PtPd@Pd core–shell nanospheres are synthesized by a one-step co-reduction method.
- This method is simple and facile, without any seed, template, or organic solvent.
- The nanocrystals exhibit the improved electrocatalytic activity towards ORR.
- The nanocrystals show the enhanced electrocatalytic activity for methanol and EG oxidation.

## GRAPHICAL ABSTRACT



## ARTICLE INFO

### Article history:

Received 22 January 2014

Received in revised form

13 March 2014

Accepted 22 April 2014

Available online 1 May 2014

### Keywords:

Bimetallic nanocrystals

Electrocatalysis

Oxygen reduction reaction

Methanol

Ethylene glycol

## ABSTRACT

Well-defined platinum–palladium@palladium core–shell nanospheres (PtPd@Pd NSs) are synthesized by a facile one-pot solution approach using *N*-methylimidazole and poly(vinyl pyrrolidone) (PVP) as directing and capping agents, respectively, without using any seed, template, or organic solvent. The coexistence of the precursors, *N*-methylimidazole, PVP, and reaction temperature has great effects on the final morphology. Thus-prepared nanocomposites display an improved electrocatalytic activity for oxygen reduction reaction (ORR) in acidic media, methanol and ethylene glycol oxidation reaction in alkaline media, compared with Pt nanoparticles, Pd nanoparticles, commercial Pt black and Pd black catalysts. This method may direct a general orientation for shape control synthesis of functional bimetallic nanocrystals as promising electrocatalysts in direct alcohol fuel cells (DAFCs).

© 2014 Elsevier B.V. All rights reserved.

## 1. Introduction

Bimetallic nanomaterials have attracted increasing interest for their widespread applications in drug delivery [1], plasmonics [2,3], chemical sensing [4,5], and surface enhanced Raman scattering [6,7]. Among them, shape-controlled synthesis attracts significant attention, because their properties strongly depend on their size, shape, composition, and crystal structures. Besides, noble metals

are known as good catalysts. Therefore, tremendous efforts have been made for preparation of bimetallic nanostructures for catalysts, such as cubes [8], wires [9], flowers [10], octahedron [11], rhombic dodecahedron [12], prism [13], dendrites [14], and high-index-faceted nanoparticles [15]. Nevertheless, their rare reserve, high price, and easy aggregation are the main challenges in practical and potential commercial applications.

To overcome these problems, noble metal is usually alloyed with a non-noble metal (rich in the Earth). To date, Pt-based bimetallic nanomaterials are considered as the most promising catalysts in fuel cells, such as Pt–Pd [16], Pt–Co [17], Pt–Ni [18], Pt–Cu [19], Pt–Ru [20], and Pt–Ag [21]. Among them, Pt–Pd nanoparticles

\* Corresponding authors. Tel./fax: +86 579 82282269.

E-mail addresses: [ajwang@zjnu.cn](mailto:ajwang@zjnu.cn) (A.-J. Wang), [jifeng@zjnu.cn](mailto:jifeng@zjnu.cn), [jifengnju@gmail.com](mailto:jifengnju@gmail.com) (J.-J. Feng).

have received particular attention for their relatively low cost and unique characteristics, compared with individual Pt or Pd nanoparticles (NPs) [22–24]. And several methods have been developed, including seed-mediated growth [22], electrochemical deposition [5], microwave refluxing [24], co-chemical reduction [25], and galvanic replacement [26]. For instance, Zhang and his co-workers prepared the Pt–Pd alloys with selective shapes under solvothermal conditions [27]. Xia et al. synthesized the Pd–Pt bimetallic nanocrystals with a concave structure by bromide-induced galvanic replacement [28].

In this report, porous core–shell Pt–Pd hybrid nanospheres (PtPd@Pd NSs) were synthesized by a simple, facile, and effective method at room temperature, without any organic solvent or seed, using *N*-methylimidazole and poly(vinyl pyrrolidone) (PVP) as directing and capping agents, respectively. The electrocatalytic activity and stability of the nanocomposites were examined by oxygen reduction reaction (ORR) in acidic media, along with methanol and ethylene glycol (EG) oxidation reaction in alkaline media.

## 2. Experimental section

### 2.1. Chemicals

Chloroplatinic acid ( $\text{H}_2\text{PtCl}_6 \cdot 6\text{H}_2\text{O}$ ), palladium chloride ( $\text{PdCl}_2$ ), PVP (MW = 58,000), *N*-methylimidazole, hydrazine hydrate (80 wt %), commercial Pt black and Pd black catalysts were purchased from Shanghai Aladdin Chemical Reagent Company (Shanghai, China). All the other chemicals were analytical grade and used without further purification. All aqueous solutions were prepared with twice-distilled water.

### 2.2. Synthesis of the porous PtPd@Pd NSs

For typical synthesis of the porous PtPd@Pd NSs, 1.29 mL of  $\text{H}_2\text{PtCl}_6$  (38.62 mM), 0.5 mL of  $\text{PdCl}_2$  (100 mM), 10 mL of PVP (0.25 wt.%), and 20  $\mu\text{L}$  of *N*-methylimidazole solutions were mixed together under stirring. Afterward, the pH of the mixed solution was adjusted to 12 by freshly prepared NaOH (0.1 M). Next, the mixture was kept at 25 °C in a water bath, followed by the addition of 100  $\mu\text{L}$  of hydrazine hydrate solution (16.5 M). The reaction mixture was quickly turned black and stirred for another 1 h in a water bath. The final black precipitate was collected by centrifugation, consecutively washed with ethanol and water, and dried at 60 °C in a vacuum for further characterization. For comparison, individual Pt and Pd NSs were prepared under the similar conditions, except only using individual  $\text{PdCl}_2$  and  $\text{H}_2\text{PtCl}_6$  as precursors, respectively.

### 2.3. Characterization

The morphology, composition, and crystal structures of the samples were characterized by transmission electron microscopy (TEM), high-resolution TEM (HRTEM), and X-ray energy dispersive spectroscopy (EDS) on a JEM-2100F HR transmission electron microscope at an accelerating voltage of 200 kV, coupled with an energy-dispersive X-ray spectrometer (Oxford-1NCA). A small amount of the black sample was dispersed in ethanol after ultrasonication, and then a drop of the diluted solution was deposited on a Cu grid for TEM observation. EDS measurements were conducted to determine the compositions of the products. The crystal structures were examined by X-ray diffraction (XRD) on a Bruker-D8-AXS diffractometer system equipped with Cu K $\alpha$  radiation (Bruker Co., Germany) and X-ray photoelectron spectroscopy by using the K-Alpha XPS spectrometer (ThermoFisher, E. Grinstead, UK) with Al K $\alpha$  X-ray radiation (1486.6 eV) for excitation.

### 2.4. Electrochemical measurements

All electrochemical experiments were performed on a CHI 660D electrochemical workstation (CH Instruments, Chenhua Co., Shanghai, China) with a conventional three-electrode cell, including a platinum wire as counter electrode, a saturated calomel electrode (SCE) as reference electrode, and a modified glassy carbon electrode (GCE, 3 mm in diameter) or a rotating disk electrode (RDE, 4 mm in diameter, Model 616) as working electrode.

For typical preparation of the modified electrode, 6.0 mg of the PtPd@Pd NSs were dispersed into 1.0 mL of water under ultrasonication for 30 min to obtain a homogeneous suspension (6.0 mg mL<sup>−1</sup>). Then, 6.0  $\mu\text{L}$  and 10  $\mu\text{L}$  of the suspension were placed on the clean GCE and RDE using a macrosyringe, respectively, followed by casting another layer of Nafion (0.05 wt %) on the electrode surface to seal the samples in place. The resulting specific loading was 0.509 mg cm<sup>−2</sup> for GCE and 0.478 mg cm<sup>−2</sup> for RDE. For comparison, Pt NSs, Pd NSs, Pt black and Pd black catalysts modified electrodes were prepared in a similar way.

Electrochemical CO-stripping voltammograms of all the samples modified GCE were recorded by oxidizing pre-adsorbed CO ( $\text{CO}_{\text{ad}}$ ) in 0.5 M  $\text{H}_2\text{SO}_4$  at a scan rate of 50 mV s<sup>−1</sup>. CO was purged through the electrolyte for 30 min to allow complete adsorption of CO onto the deposit. The amount of the  $\text{CO}_{\text{ad}}$  was evaluated by integrating the  $\text{CO}_{\text{ad}}$  stripping peak and correcting for the capacitance of the double electric layer. Meanwhile, the ORR measurements were carried out in O<sub>2</sub>-saturated 0.5 M  $\text{H}_2\text{SO}_4$  at a scan rate of 5 mV s<sup>−1</sup> on the modified RDE. The cyclic voltammetric and chronoamperometric experiments of all the samples modified GCE were carried out in 1.0 M KOH at a scan rate of 50 mV s<sup>−1</sup>, using methanol and EG oxidation reactions as model systems. All the experiments were performed at room temperature, if not stated otherwise.

## 3. Results and discussion

### 3.1. Characterization

The morphologies of the typical samples were characterized by TEM images (Fig. 1). There are a lot of well-defined core–shell NSs with a narrow size distribution, where their inner parts are darker than the outside parts (Fig. 1A). HRTEM images reveal that each nanosphere displays dandelion-like porous nanostructures (Fig. 1B–C). Besides, its outside parts are assembled by numerous branched subunits. Moreover, the interplanar distance is calculated to be ca. 0.22 nm at most regions of the outside regions (Fig. 1C), which is in good accordance with the (111) planes of Pt–Pd alloy [29]. The SAED pattern depicts polycrystalline nature of the PtPd@Pd NSs (Fig. 1D) [30,31]. The EDS mapping (Fig. 2A–C) and line scanning profiles (Fig. 2D) were manipulated to examine the distribution of Pt and Pd, in which both Pt and Pd are homogeneously distributed at the center part, showing the formation of PtPd hybrid as core with high density. Meanwhile, the diameter of the Pd sphere is much larger than that of the Pt sphere, suggesting that the shell is mainly predominated by Pd element [32].

XRD spectra (Fig. 3B) were provided to further identify the crystal structure and chemical composition of the PtPd@Pd NSs, in which the representative peaks at 40.1°, 46.7°, 68.1°, and 82.3° are well indexed to the (111), (200), (220), and (311) planes of the face-centered-cubic (fcc) Pt–Pd alloy [33], respectively, as strongly supported by the EDS (Fig. 3A) and SAED (Fig. 1D) experiments. Importantly, the representative diffraction peaks are broadened, demonstrating smaller dimensions of the hybrid nanocrystals. Furthermore, these peaks are coincidentally located between standard XRD pattern positions of Pt (JCPDS-04-0802 Pt) and Pd (JCPDS-

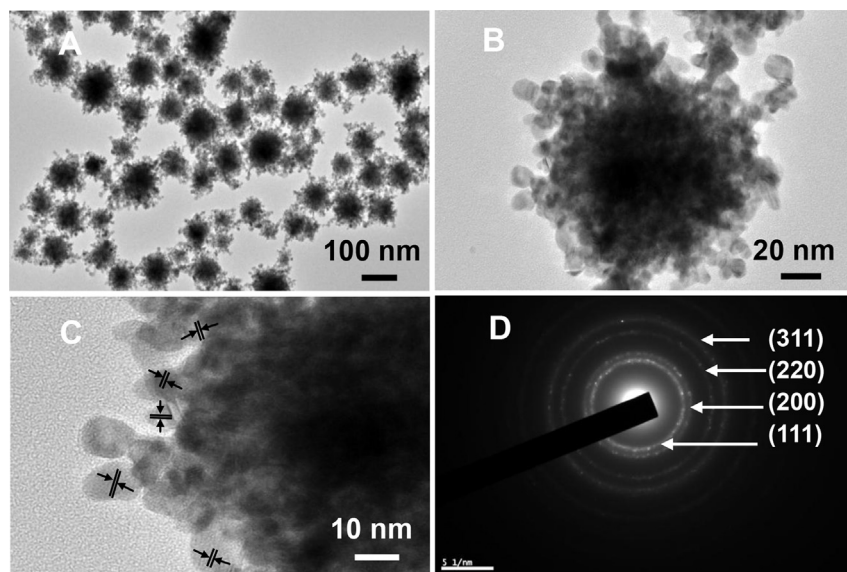


**Fig. 1.** Low (A) and high (B, C) magnification TEM images of the PtPd@Pd NSs. The corresponding SAED pattern (D).

46–1043 Pd), confirming the formation of Pt–Pd alloy [34]. Additionally, similar peak positions are found for the standard XRD patterns of individual Pt and Pd, leading to the difficulty to distinguish their peaks [35].

XPS analysis is widely used to check the valence states and surface composition of a catalyst [36]. As illustrated in Fig. 3C and D, high-resolution Pt 4f and Pd 3d spectra are offered to clarify the composition and surface chemical states of the Pt–Pd NSs. Specifically, Pt 4f can be deconvoluted into two pairs of peaks (Fig. 3C). The most intense doublet at 71.42 eV (Pt 4f<sub>7/2</sub>) and 74.86 eV (Pt 4f<sub>5/2</sub>) are the characteristic peaks of the metallic Pt. The other weaker ones at the 72.38 eV (Pt 4f<sub>7/2</sub>) and 76.35 eV (Pt 4f<sub>5/2</sub>) can be attributed to Pt<sup>II</sup> species in the forms of PtO and PtOH [37]. Meanwhile, the Pd 3d peak can be separated into two pairs of peaks (Fig. 3D), i.e., 335.44 eV (Pd 3d<sub>3/2</sub>), 340.73 eV (Pd 3d<sub>3/2</sub>), 342.53 eV (Pd 3d<sub>5/2</sub>), and 337.55 eV (Pd 3d<sub>5/2</sub>), which are assigned to metallic Pd<sup>0</sup> and Pd<sup>II</sup> [38], respectively. By measuring the relative peak

intensities, it is found that Pt<sup>0</sup> and Pd<sup>0</sup> are the predominant species, revealing complete reduction of the two precursors [25]. Additionally, the predominant Pt<sup>0</sup> and Pd<sup>0</sup> species can enhance the electrocatalytic activity of Pt-based catalysts, as confirmed by the previous work [39], which revealed that the chemical state of Pt is vital for determining the electrocatalytic activity.

To have a deep insight on the formation mechanism of the PtPd@Pd NSs, a series of control experiments were performed. Impressively, porous PtPd@Pd NSs structures are emerged with suitable amount of *N*-methylimidazole, whereas the core–shell nanostructures are hardly obtained without (Fig. 4A) and with excessive *N*-methylimidazole (Fig. 4B–D), revealing the key role of *N*-methylimidazole for fabrication of the porous PtPd@Pd NSs, probably owing to preferential adsorption of *N*-methylimidazole on the Pt–Pd alloy surface [40]. Similarly, the absence of PVP yields some porous aggregates (Fig. S1A, Supporting information), and the increase of the PVP amount is contributed to well dispersion of the

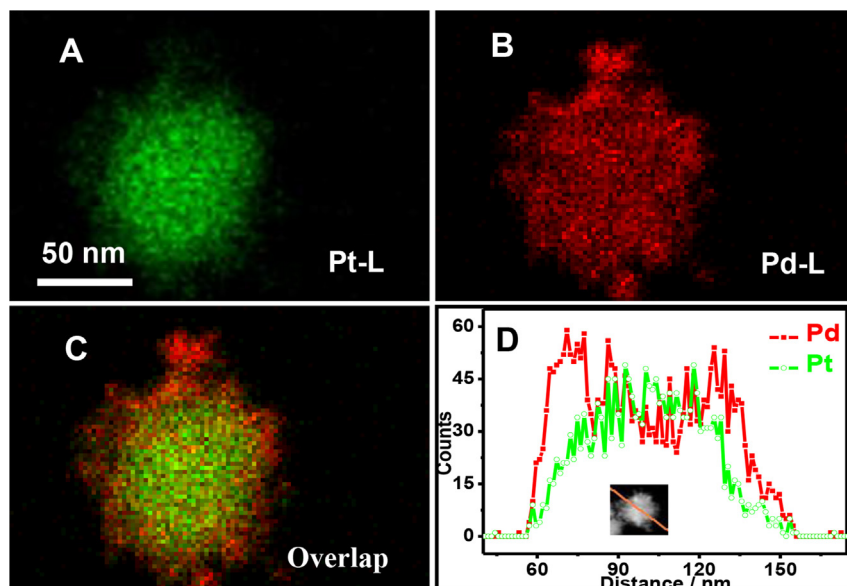


**Fig. 2.** The EDS mapping (A–C) and line scanning profiles (D) of the PtPd@Pd NSs.

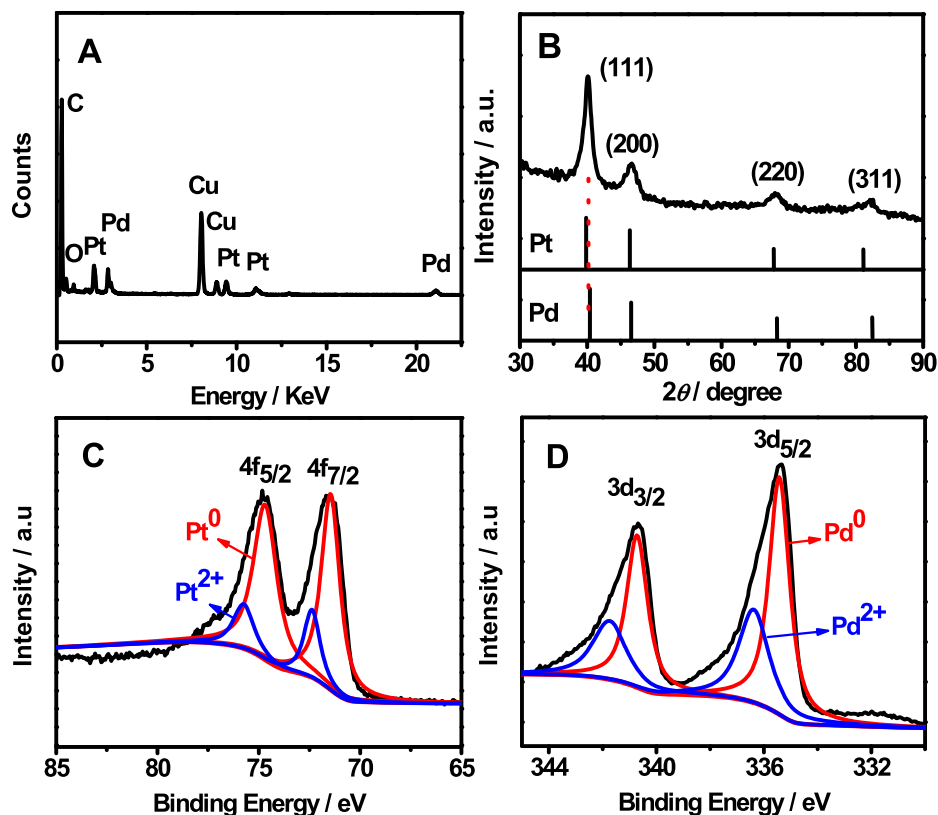


Fig. 3. EDS (A), XRD (B), high-resolution Pt 4f (C) and Pd 3d XPS (D) spectra of the PtPd@Pd NSs.

Pt–Pd nanostructures with improved quality (Fig. S1B, C, Supporting information), verifying the anti-aggregation role of PVP [41]. Considering the ease operation, 0.25 wt % is chosen in the following experiments.

The molar ratio of Pt to Pd precursors (Pt/Pd) was one of the essential factors in the present synthesis [10]. As expected, uniform solid Pd NSs and irregular porous sponge-like Pt NSs are generated using individual  $\text{PdCl}_2$  (Fig. S2A, Supporting information) and  $\text{H}_2\text{PtCl}_6$  (Fig. S2B, Supporting information) as precursors,

respectively, while other conditions are kept unchanged. Similar nanostructures are observed by increasing the Pt/Pd molar ratio from 1:1 to 2:1, while their quality are clearly decreased (Fig. S2C, Supporting information), confirming that the strong binding affinity of  $\text{PtCl}_6^{2-}$  ions to *N*-containing molecules (*N*-methylimidazole and PVP) induces the formation of highly porous morphology, compared with that of  $\text{Pd}^{2+}$  ions [42]. Alternatively, decreasing the Pt/Pd molar ratio to 1:2 produces some irregular loose aggregates (Fig. S2D, Supporting information). This is due to the low inductive

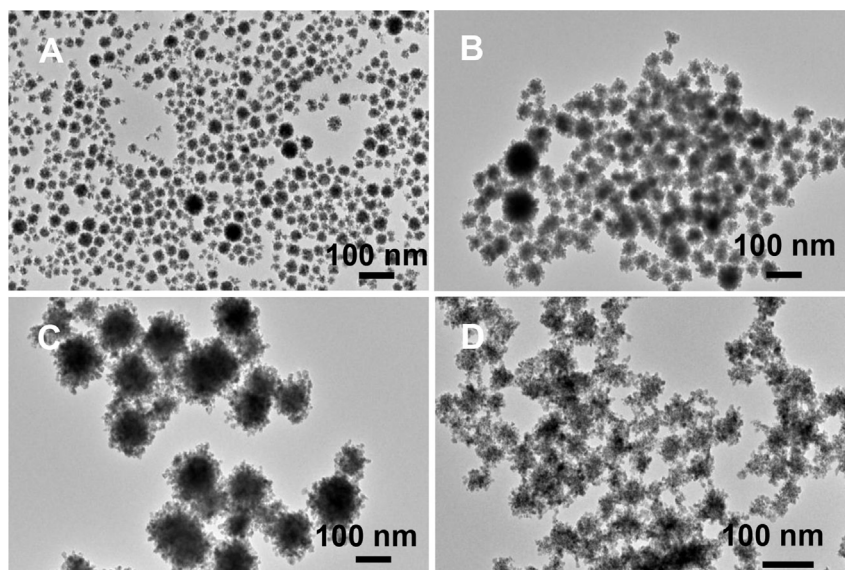


Fig. 4. TEM images of the products obtained without (A), and with 10 mM (B), 50 mM (C), and 100 mM (D) *N*-methylimidazole.



capacity of insufficient Pt content. On the other hand, considering the different standard reduction potential of Pt and Pd ions ( $\text{PtCl}_6^{2-}/\text{Pt}$ , 0.73 V,  $\text{Pd}^{2+}/\text{Pd}$ , 0.915 V), it might deduce that the Pd particles firstly nucleate [43], causing the formation of the Pd cores in the innermost site of the PtPd@Pd NSs (Fig. 2C, D).

Besides, the reaction temperature and pH value are also critical to the synthesis of the porous PtPd@Pd NSs. Specifically, the quality of the porous NSs is decreased by using low (Fig. S3A, Supporting information) or high (Fig. S3B, Supporting information) temperature. Furthermore, the porous NSs are hardly obtained by further increasing the temperature to 60 °C (Fig. S3C, Supporting

information) or 80 °C (Fig. S3D, Supporting information), owing to the enlarged deviation from the equilibrium state [44,45]. These results indicate that the PtPd@Pd NSs can be formed in the suitable temperature range. Similarly, the variation of the pH value ranging from 2 to 7 in the reaction media brings random assembly of NSs with poor dispersity and bad quality (Fig. S4A, B, Supporting information), indicating that the pH is important to control the shape of the Pt–Pd alloy, which may be ascribed to the variation of adsorbability on the Pt–Pd nanoparticles surface with the protonation or deprotonation of the adsorbed molecules by changing the pH values [46].

Herein, the time-dependent experiments were performed to explain the formation of porous PtPd@Pd NSs (Fig. 5). Upon the introduction of hydrazine hydrate to the reaction media, most of the Pt and Pd precursors were quickly reduced to metallic Pt and Pd atoms in 1 min, leading to the formation of Pt–Pd hybrid core with high density (Fig. 5A). Within 5 min, under the directing and capping effects of *N*-methylimidazole and PVP, the newly generated Pt and Pd atoms attached along the core edges to minimize the total surface free energy of the system (Fig. 5B), through the anisotropic growth and the diffusion-limit process [47,48]. Meanwhile, the inductive effects of  $\text{PtCl}_6^{2-}$  ions to *N*-containing molecules (*N*-methylimidazole and PVP) led to the formation of the porous structure as above mentioned. As the reaction time proceeded, the Pd nanoparticles exposed over the shells of the PtPd@Pd NSs to keep the whole NSs stable (Fig. 2C), which could be due to the lower interfacial energy of metallic Pd ( $2.05 \text{ J m}^{-2}$ ) than that of Pt ( $2.48 \text{ J m}^{-2}$ ) [49,50]. The PtPd@Pd NSs were almost formed as the reaction time proceeded to 30 min (Fig. 5C). Further prolonging the reaction time to 1 h produced the PtPd@Pd NSs with improved quality (Fig. 1). As a result, the present formation mechanism includes two processes of rapid nucleation and particle directing attachment [18,51–53].

### 3.2. Electrochemical measurements

The CO-stripping voltammograms of the PtPd@Pd NSs (Fig. 6), Pt NSs (Fig. S5, curve a, Supporting information), Pd (Fig. S5, curve b, Supporting information), commercial Pt black (Fig. S5, curve c, Supporting information) and Pd black (Fig. S5, curve d, Supporting information) catalysts modified electrodes were recorded in 0.5 M  $\text{H}_2\text{SO}_4$  to examine the corresponding electrochemically active

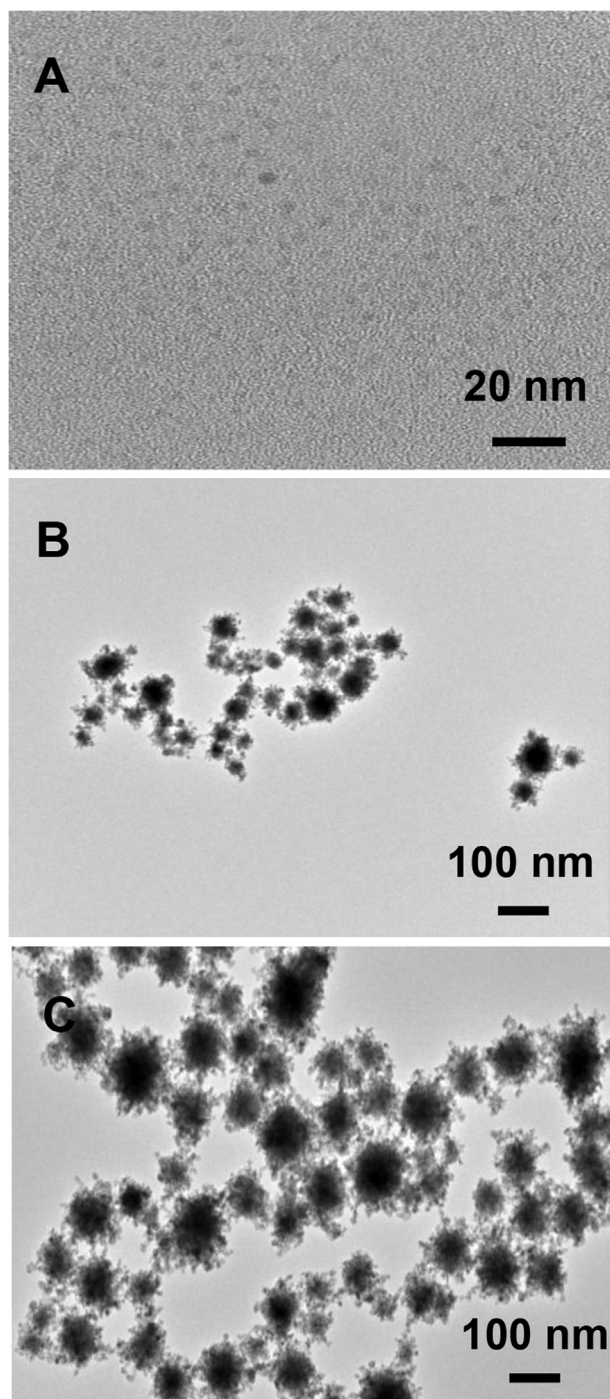


**Fig. 5.** TEM images of the Pt–Pd alloy nanocrystals prepared at different reaction time: 1 min (A), 5 min (B), and 30 min (C).

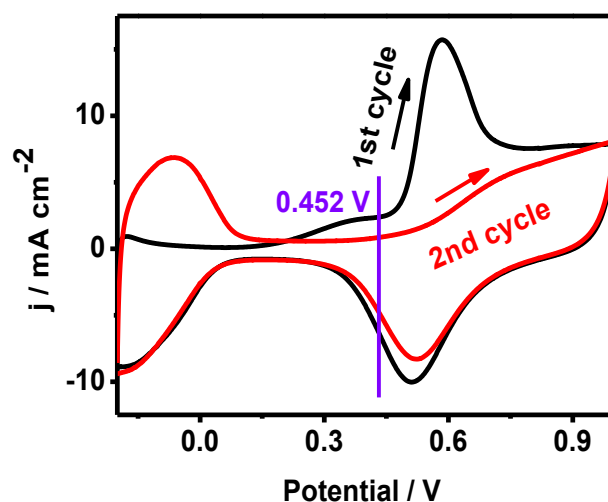


**Fig. 6.** The CO-stripping voltammograms of the PtPd@Pd NSs modified electrode in 0.5 M  $\text{H}_2\text{SO}_4$  at a scan rate of  $50 \text{ mV s}^{-1}$ .

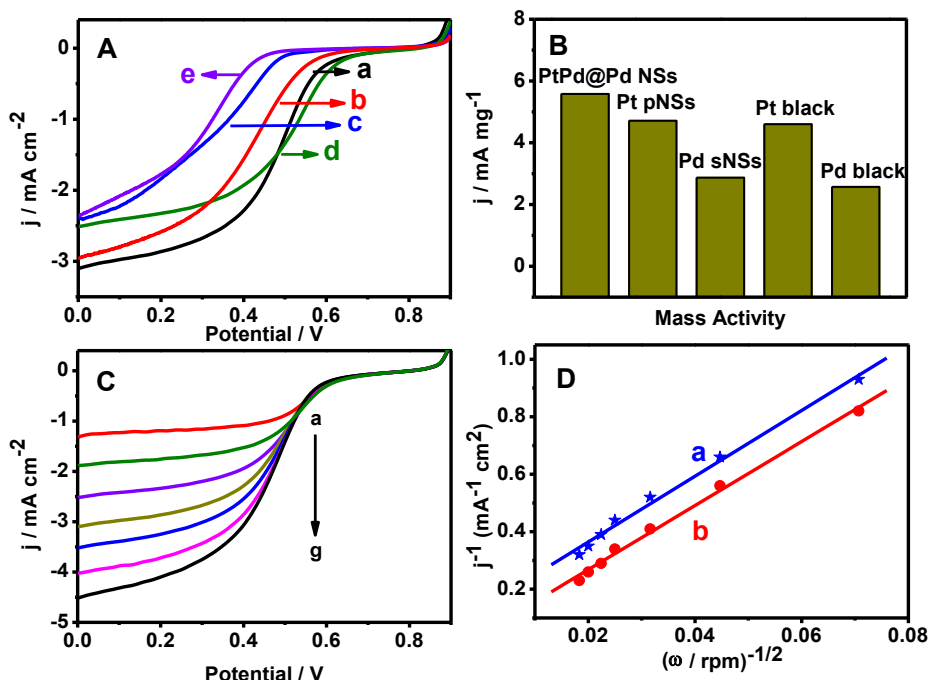


**Fig. 7.** The LSVs (A) of the PtPd@Pd NSs (curve a), Pt NSs (curve b), Pd NSs (curve c), Pt black (curve d) and Pd black (curve e) catalysts modified electrodes in  $O_2$ -saturated 0.5 M  $H_2SO_4$  at a scan rate of  $5 \text{ mV s}^{-1}$  with a rotating rate of 1600 rpm. The corresponding mass activity (B) at the applied potential of 0.3 V. The LSVs (C) of the PtPd@Pd NSs modified electrode in  $O_2$ -saturated 0.5 M  $H_2SO_4$  at a scan rate of  $5 \text{ mV s}^{-1}$  with different rotating rate (curves a–g): 200, 500, 1000, 1600, 2000, 2500, and 3000 rpm. The K-L plots (D) of the PtPd@Pd NSs modified electrode for  $O_2$  reduction at 0.4 V (curve a) and 0.1 V (curve b).

surface area (EASA) [54,55]. As shown in Fig. 6, the CO-stripping peak is emerged at 0.6 V for the PtPd@Pd NSs, located between Pt black (0.55 V) and Pd black (0.65 V) catalysts, further confirming the formation of Pt–Pd alloy. The EASA is  $29.72 \text{ m}^2 \text{ g}^{-1}$  for the PtPd@Pd NSs, which is significantly larger than those of the Pt NSs

( $15.82 \text{ m}^2 \text{ g}^{-1}$ ), Pd NSs ( $1.89 \text{ m}^2 \text{ g}^{-1}$ ), Pt black ( $6.99 \text{ m}^2 \text{ g}^{-1}$ ) and Pd black ( $11.59 \text{ m}^2 \text{ g}^{-1}$ ) catalysts, suggesting larger active surface area and higher electrocatalytic activity of the PtPd@Pd NSs [56].

To test the electrocatalytic activity of the PtPd@Pd NSs, ORR measurements were firstly performed using the Pt NSs, Pd NSs,

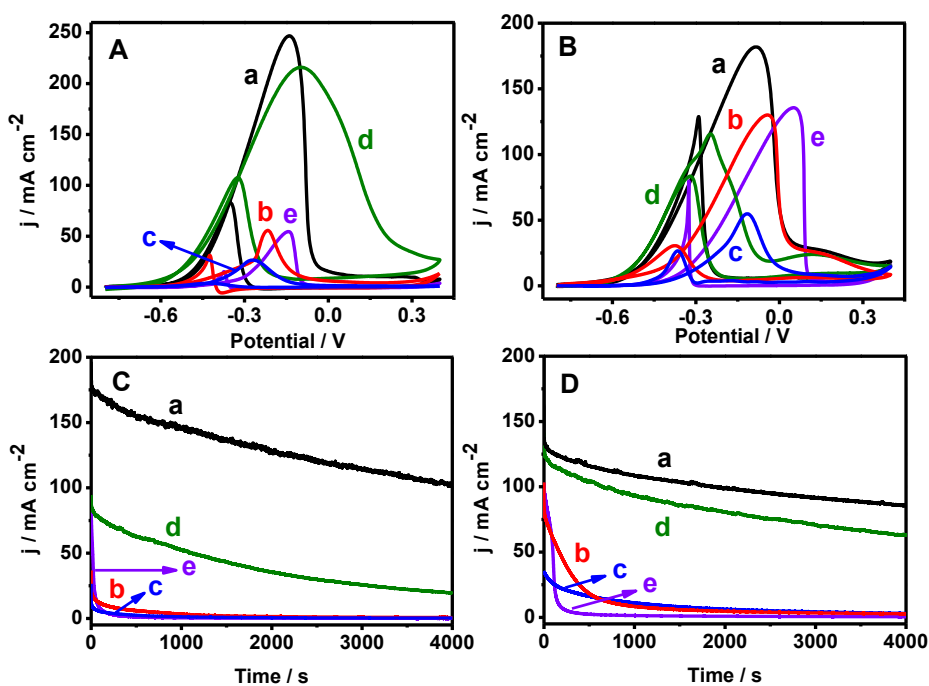


**Fig. 8.** The cyclic voltammograms of the PtPd@Pd NSs (curve a), Pt NSs (curve b), Pd NSs (curve c), Pt black (curve d) and Pd black (curve e) catalysts modified electrodes in 1.0 M KOH + 1.0 M methanol (A) and 1.0 M KOH + 1.0 M EG (B) at a scan rate of  $50 \text{ mV s}^{-1}$ . The chronoamperometric curves of the PtPd@Pd NSs (curve a), Pt NSs (curve b), Pd NSs (curve c), Pt black (curve d) and Pd black (curve e) catalysts modified electrodes in 1.0 M KOH + 1.0 M methanol (C) and 1.0 M KOH + 1.0 M EG (D) at an applied potential of  $-0.2 \text{ V}$ .

commercial Pt black and Pd black catalysts as references. It's distinct that the current densities of the PtPd@Pd NSs in the hydrogen adsorption/desorption and oxide formation/reduction regions are much higher than that of the Pt NSs, Pd NSs, Pt black and Pd black catalysts (Fig. S6, Supporting information), further revealing the enhanced electrocatalytic activity of the PtPd@Pd NSs [57].

ORR is an important reaction in fuel cells and oxygen sensors, which involves the process of breaking of the O–O bonds and the formation of the O–H groups [58,59]. Fig. 7A shows the linear sweep voltammograms (LSVs) of the PtPd@Pd NSs (curve a), Pt NSs (curve b), Pd NSs (curve c), Pt black (curve d) and Pd black (curve e) catalysts modified electrodes. In the case of the PtPd@Pd NSs, a remarkable enhanced catalytic current is observed at 0.64 V, which is ascribed to the reduction of oxygen [57]. Meanwhile, the onset potential is similar to the Pt NSs and Pt black catalysts, but much more positive than those of the Pd NSs and Pd black catalysts, indicating the improved electrocatalytic activity of the PtPd@Pd NSs [60].

The ORR kinetic currents ( $i_k$ ) were normalized by calculating to the mass loading of catalysts (Fig. 7B) at 0.3 V. Clearly, the current densities on the PtPd@Pd NSs are higher than those of the Pt NSs, Pd NSs, Pt black and Pd black catalysts in the mass activity, manifesting the improved performance of the PtPd@Pd NSs under the identical conditions [25,28].

To investigate the ORR electron transfer kinetics, the LSVs of the PtPd@Pd NSs modified electrode was recorded in O<sub>2</sub>-saturated 0.5 M H<sub>2</sub>SO<sub>4</sub> with different electrode rotating rates (Fig. 7C). The corresponding Koutechy–Levich (K–L) plots were also obtained at the potential of 0.4 V (Fig. 7D, curve a) and 0.1 V (Fig. 7D, curve b) [61]. Based on the slope of the K–L plots [57,62], the value of the electron transfer number at the potential of 0.4 V and 0.1 V are evaluated to be 4.3 and 4.1 respectively, implying a predominantly 4-electron reduction pathway where O<sub>2</sub> is directly reduced to H<sub>2</sub>O. The enhanced kinetic current density and high electron transfer number demonstrate the PtPd@Pd NSs as a fascinating ORR catalyst.

Fig. 8 shows the results of the PtPd@Pd NSs (curve a), Pt NSs (curve b), Pd NSs (curve c), Pt black (curve d), and Pd black (curve e) catalysts modified electrodes for methanol and EG oxidation reaction. For methanol oxidation, the current density of the PtPd@Pd NSs modified electrode is 248 mA cm<sup>−2</sup>, which is much larger than those of the Pt NSs (57.05 mA cm<sup>−2</sup>), Pd NSs (27.95 mA cm<sup>−2</sup>), Pt black (213 mA cm<sup>−2</sup>) and Pd black (53 mA cm<sup>−2</sup>) catalysts under the same conditions (Fig. 8A). Moreover, this value is higher than that of the Pt/PdCu nanoboxes modified electrode [63]. Meanwhile, the onset potential of the PtPd@Pd NSs is emerged at around −0.6 V, which is close to the Pt NSs (−0.63 V) and Pt black (−0.62 V) catalysts, but more negative than those of Pd NSs (−0.55 V) and Pd black (−0.45 V) catalysts.

On the other hand, the ratio of the forward ( $j_F$ ) to the reverse ( $j_R$ ) peak current densities of the PtPd@Pd NSs is 3.07, which is similar to that of the Pd black catalyst (3.31), but larger than that of the Pt NSs (1.79) and Pt black (1.98) catalysts. Besides, this value is a little higher than that of the PtCu<sub>3</sub> cubic nanocages (1.93) in the literature [19]. In the case of EG oxidation, a similar trend was observed where the PtPd@Pd NSs showed the highest electrocatalytic current density among all the catalysts (Fig. 8B). These results indicate the enhanced electrocatalytic activity of the PtPd@Pd NSs, owing to their superior CO tolerance and larger surface area resulting from the porous nanostructures and the synergetic effects of Pt and Pd [43,64].

The durability of the PtPd@Pd NSs (curve a), Pt NSs (curve b), Pd NSs (curve c), Pt black (curve d) and Pd black (curve e) catalysts modified electrodes were investigated by chronoamperometry in

alkaline media containing methanol (Fig. 8C) and EG (Fig. 8D). For both methanol and EG oxidation, the current densities of the PtPd@Pd NSs are higher than those of the Pt NSs, Pd NSs, Pt black and Pd black catalysts during the entire time course, demonstrating long-term stability of the PtPd@Pd NSs [65,66].

#### 4. Conclusions

We have developed a simple and facile method for preparation of the porous PtPd@Pd NSs at room temperature, without using any seed or organic solvent, using *N*-methylimidazole and PVP as the directing and capping agents, respectively. The PtPd@Pd NSs were formed via rapid nucleation and particle directing attachment processes. The as-prepared nanocomposites showed the enhanced electrocatalytic activity and better stability towards ORR, methanol and ethylene glycol oxidation reaction, compared with Pt NSs, Pd NSs, commercial Pt black and Pd black catalysts. This synthesis strategy might be extended to fabricate other metallic alloys, which can be used as anode and cathode electrocatalysts in DAFCs.

#### Acknowledgments

This work was financially supported by the National Natural Science Foundation of China (21175118, 21275130 and 21275131) and Zhejiang Province University Young Academic Leaders of Academic Climbing Project (No. pd2013055).

#### Appendix A. Supplementary data

Supplementary data related to this article can be found at <http://dx.doi.org/10.1016/j.jpowsour.2014.04.108>.

#### References

- [1] J. Liu, S.Z. Qiao, J.S. Chen, X.W. Lou, X. Xing, G.Q. Lu, *Chem. Commun.* 47 (2011) 12578–12591.
- [2] M.B. Cortie, A.M. McDonagh, *Chem. Rev.* 111 (2011) 3713–3735.
- [3] W. He, X. Wu, J. Liu, X. Hu, K. Zhang, S. Hou, W. Zhou, S. Xie, *Chem. Mater.* 22 (2010) 2988–2994.
- [4] X. Niu, C. Chen, H. Zhao, Y. Chai, M. Lan, *Biosens. Bioelectron.* 36 (2012) 262–266.
- [5] S. Cao, L. Zhang, Y. Chai, R. Yuan, *Biosens. Bioelectron.* 42 (2013) 532–538.
- [6] K. Kim, K.L. Kim, K.S. Shin, *J. Phys. Chem. C* 115 (2011) 23374–23380.
- [7] Z. Jiang, Q. Zhang, C. Zong, B.-J. Liu, B. Ren, Z. Xie, L. Zheng, *J. Mater. Chem.* 22 (2012) 18192–18197.
- [8] M. Chen, J. Kim, J.P. Liu, H. Fan, S. Sun, *J. Am. Chem. Soc.* 128 (2006) 7132–7133.
- [9] B.Y. Xia, H.B. Wu, Y. Yan, X.W. Lou, X. Wang, *J. Am. Chem. Soc.* 135 (2013) 9480–9485.
- [10] J. Xu, A.R. Wilson, A.R. Rathmell, J. Howe, M. Chi, B.J. Wiley, *ACS Nano* 5 (2011) 6119–6127.
- [11] C. Cui, L. Gan, H.-H. Li, S.-H. Yu, M. Heggen, P. Strasser, *Nano Lett.* 12 (2012) 5885–5889.
- [12] Y.W. Lee, M. Kim, S.W. Kang, S.W. Han, *Angew. Chem.* 123 (2011) 3528–3532.
- [13] S.I. Lim, M. Varón, I. Ojea-Jiménez, J. Arbiol, V. Puentes, *Chem. Mater.* 22 (2010) 4495–4504.
- [14] Y.W. Lee, D. Kim, J.W. Hong, S.W. Kang, S.B. Lee, S.W. Han, *Small* 9 (2013) 660–665.
- [15] Z. Quan, Y. Wang, J. Fang, *Acc. Chem. Res.* 46 (2012) 191–202.
- [16] I. Choi, S.H. Ahn, J.J. Kim, O.J. Kwon, *Appl. Catal. B* 102 (2011) 608–613.
- [17] S. Guo, D. Li, H. Zhu, S. Zhang, N.M. Markovic, V.R. Stamenkovic, S. Sun, *Angew. Chem. Int. Ed.* 52 (2013) 3465–3468.
- [18] W. Wang, D. Wang, X. Liu, Q. Peng, Y. Li, *Chem. Commun.* 49 (2013) 2903–2905.
- [19] B.Y. Xia, H.B. Wu, X. Wang, X.W. Lou, *J. Am. Chem. Soc.* 134 (2012) 13934–13937.
- [20] C. Xu, L. Wang, X. Mu, Y. Ding, *Langmuir* 26 (2010) 7437–7443.
- [21] C. Li, Y. Yamauchi, *Phys. Chem. Chem. Phys.* 15 (2013) 3490–3496.
- [22] B. Lim, M. Jiang, P.H.C. Camargo, E.C. Cho, J. Tao, X. Lu, Y. Zhu, Y. Xia, *Science* 324 (2009) 1302–1305.
- [23] Y. Lu, Y. Jiang, H. Wu, W. Chen, *J. Phys. Chem. C* 117 (2013) 2926–2938.
- [24] H. Zhang, Y. Yin, Y. Hu, C. Li, P. Wu, S. Wei, C. Cai, *J. Phys. Chem. C* 114 (2010) 11861–11867.

- [25] G. Fu, K. Wu, J. Lin, Y. Tang, Y. Chen, Y. Zhou, T. Lu, J. Phys. Chem. C 117 (2013) 9826–9834.
- [26] W. Zhang, M. Wang, J. Chen, T. Romeo, A.T. Harris, A.I. Minett, Electrochem. Commun. 34 (2013) 73–76.
- [27] Z.-C. Zhang, J.-F. Hui, Z.-G. Guo, Q.-Y. Yu, B. Xu, X. Zhang, Z.-C. Liu, C.-M. Xu, J.-S. Gao, X. Wang, Nanoscale 4 (2012) 2633–2639.
- [28] H. Zhang, M. Jin, J. Wang, W. Li, P.H.C. Camargo, M.J. Kim, D. Yang, Z. Xie, Y. Xia, J. Am. Chem. Soc. 133 (2011) 6078–6089.
- [29] J.W. Hong, S.W. Kang, B.-S. Choi, D. Kim, S.B. Lee, S.W. Han, ACS Nano 6 (2012) 2410–2419.
- [30] Y.-W. Lee, A.R. Ko, S.-B. Han, H.-S. Kim, K.-W. Park, Phys. Chem. Chem. Phys. 13 (2011) 5569–5572.
- [31] Y. Yamauchi, A. Tonegawa, M. Komatsu, H. Wang, L. Wang, Y. Nemoto, N. Suzuki, K. Kuroda, J. Am. Chem. Soc. 134 (2012) 5100–5109.
- [32] J.W. Hong, Y.W. Lee, M. Kim, S.W. Kang, S.W. Han, Chem. Commun. 47 (2011) 2553–2555.
- [33] H. Liao, Y. Hou, Chem. Mater. 25 (2013) 457–465.
- [34] S. Guo, S. Zhang, D. Su, S. Sun, J. Am. Chem. Soc. 135 (2013) 13879–13884.
- [35] V.L. Nguyen, M. Ohtaki, T. Matsubara, M.T. Cao, M. Nogami, J. Phys. Chem. C 116 (2012) 12265–12274.
- [36] Y. Lu, Y. Jiang, W. Chen, Nano Energy 2 (2013) 836–844.
- [37] J. Yang, W. Zhou, C.H. Cheng, J.Y. Lee, Z. Liu, ACS Appl. Mater. Interfaces 2 (2009) 119–126.
- [38] X. Yang, Q. Yang, J. Xu, C.-S. Lee, J. Mater. Chem. 22 (2012) 8057–8062.
- [39] S. Sharma, A. Ganguly, P. Papakonstantinou, X. Miao, M. Li, J.L. Hutchison, M. Delichatsios, S. Ukleja, J. Phys. Chem. C 114 (2010) 19459–19466.
- [40] X. Huang, E. Zhu, Y. Chen, Y. Li, C.-Y. Chiu, Y. Xu, Z. Lin, X. Duan, Y. Huang, Adv. Mater. 25 (2013) 2974–2979.
- [41] Z. Niu, Y. Li, Chem. Mater. 26 (2013) 72–83.
- [42] S.W. Kang, Y.W. Lee, Y. Park, B.-S. Choi, J.W. Hong, K.-H. Park, S.W. Han, ACS Nano 7 (2013) 7945–7955.
- [43] L. Wang, Y. Nemoto, Y. Yamauchi, J. Am. Chem. Soc. 133 (2011) 9674–9677.
- [44] L.-M. Lacroix, C. Gatel, R. Arenal, C. Garcia, S. Lachaize, T. Blon, B. Warot-Fonrose, E. Snoeck, B. Chaudret, G. Viau, Angew. Chem. Int. Ed. 51 (2012) 4690–4694.
- [45] H. Jia, X. Bai, L. Zheng, CrystEngComm 14 (2012) 2920–2925.
- [46] H. Zhang, B. Chen, J.F. Banfield, J. Phys. Chem. C 114 (2010) 14876–14884.
- [47] Y. Wang, S.-I. Choi, X. Zhao, S. Xie, H.-C. Peng, M. Chi, C.Z. Huang, Y. Xia, Adv. Funct. Mater. 24 (2013) 131–139.
- [48] B. Lim, M. Jiang, T. Yu, P.C. Camargo, Y. Xia, Nano Res. 3 (2010) 69–80.
- [49] J. Chai, F. Li, Y. Hu, Q. Zhang, D. Han, L. Niu, J. Mater. Chem. 21 (2011) 17922–17929.
- [50] A.-X. Yin, X.-Q. Min, Y.-W. Zhang, C.-H. Yan, J. Am. Chem. Soc. 133 (2011) 3816–3819.
- [51] S. Rastegarzadeh, S. Abdali, Talanta 104 (2013) 22–26.
- [52] B. Lim, Y. Xia, Angew. Chem. Int. Ed. 50 (2011) 76–85.
- [53] L. Wang, Y. Yamauchi, Chem. Mater. 21 (2009) 3562–3569.
- [54] A.-J. Wang, F.-F. Li, J.-N. Zheng, H.-X. Xi, Z.-Y. Meng, J.-J. Feng, RSC Adv. 3 (2013) 10355–10362.
- [55] A.U. Nilekar, K. Sasaki, C.A. Farberow, R.R. Adzic, M. Mavrikakis, J. Am. Chem. Soc. 133 (2011) 18574–18576.
- [56] X. Yang, X. Liu, X. Meng, X. Wang, G. Li, C. Shu, L. Jiang, C. Wang, J. Power Sources 240 (2013) 536–543.
- [57] Q.-L. Zhang, T.-Q. Xu, J. Wei, J.-R. Chen, A.-J. Wang, J.-J. Feng, Electrochim. Acta 112 (2013) 127–132.
- [58] V.R. Stamenkovic, B. Fowler, B.S. Mun, G. Wang, P.N. Ross, C.A. Lucas, N.M. Markovic, Science 315 (2007) 493–497.
- [59] J. Zhang, Y. Mo, M.B. Vukmirovic, R. Klie, K. Sasaki, R.R. Adzic, J. Phys. Chem. B 108 (2004) 10955–10964.
- [60] Y.-N. Wu, S.-J. Liao, Z.-X. Liang, L.-J. Yang, R.-F. Wang, J. Power Sources 194 (2009) 805–810.
- [61] Z. Jiang, Z.-J. Jiang, X. Tian, W. Chen, J. Mater. Chem. A 2 (2014) 441–450.
- [62] G. Srourov, K.S. Ranjan, C.R. Raj, Nanotechnology 23 (2012) 385602–385610.
- [63] C. Hu, H. Cheng, Y. Zhao, Y. Hu, Y. Liu, L. Dai, L. Qu, Adv. Mater. 24 (2012) 5493–5498.
- [64] S.-S. Li, J.-J. Lv, Y.-Y. Hu, J.-N. Zheng, J.-R. Chen, A.-J. Wang, J.-J. Feng, J. Power Sources 247 (2013) 213–218.
- [65] Y. Zhao, X. Yang, J. Tian, F. Wang, L. Zhan, Int. J. Hydrogen Energy 35 (2010) 3249–3257.
- [66] S. Guo, S. Zhang, X. Sun, S. Sun, J. Am. Chem. Soc. 133 (2011) 15354–15357.